Long Range Order in Polymeric Micelles under Steady Shear

Glen A. McConnell,[†] Min Y. Lin,[‡] and Alice P. Gast*,[†]

Department of Chemical Engineering, Stanford University, Stanford, California 94305-5025, and Exxon Research and Engineering Corporation, Annandale, New Jersey 08801

ABSTRACT: Small angle neutron scattering (SANS) experiments were performed to examine the long range order in polymeric, micellar crystals subjected to linear steady shear. Polystyrene/polyisoprene (PS/PI) diblocks with varying degrees of polymerization and block asymmetry are used to generate both body-centered (BCC) and face-centered (FCC) cubic micellar crystals when suspended in decane. The FCC crystals show a transition from polycrystallinity to ⟨111⟩ sliding layers. This transition is marked by a significant hysteresis in the steady shear stress versus shear rate data. For higher shear rates, we observe ⟨111⟩ layers normal to the shear gradient slipping past each other. As the shear rate increases, the layers do not hop perfectly from one registry site to the next. The BCC crystals subjected to linear shear demonstrate a more continuous deformation of the local crystalline lattice that eventually develops into a BCC twin structure with the ⟨110⟩ layers normal to the shear gradient. The BCC twins advance in portions along the twinning planes, allowing the crystal to flow at moderate shear rates. At higher shear rates we observe a loss of long range order associated with shear melting. These results show an interesting similarity to other cubic crystals observed in both colloids and diblock melts.

1. Introduction

The uncertainty surrounding the nature of a crystal's microstructural evolution and the link to its rheological response, as well as the possibility for long-lived metastable states formed upon preshearing, motivate our interest in the long range order of polymeric micelles subjected to a steady shear. Ackerson and co-workers'[1–6] pioneering research on flowing colloidal crystals identified some of their major microstructural transitions. These researchers and others have applied molecular-based theories to understand the structural transitions observed under steady shear as well as establishing links to the macroscopic rheological response.[7–10] Nonequilibrium molecular dynamics simulations ignoring hydrodynamic interactions have attempted to capture some of these features.[11]

Despite these efforts, relatively few experiments have focused on polymeric, micellar systems. One such example includes Mortensen's small angle neutron scattering (SANS) experiments on polyethylene oxide/polypropylene (PEO/PPO/PEO) triblocks in water.[12] The hydrophobicity of the PPO block is strongly temperature dependent, and they exploit this feature to produce micellar crystals. These researchers utilize shear to achieve macroscopic alignment to generate a diffraction image suitable for crystallographic identification. When the temperature in their sample is increased, the PPO block becomes increasingly hydrophobic, causing the diblocks to ultimately self-assemble into micelles and form a body-centered cubic (BCC) array observed in the SANS diffraction images. Another example involves experiments performed by Higgins[13] on polystyrene/polyethylene propylene (PS/PEP) diblock micelles in dodecane. Higgins and co-workers subject their samples to shear rates high enough to observe the loss of long range order associated with shear melting. While they observe shear dependent microstructures, the experiments and analysis focus on the shear melting behavior and prevent a more general interpretation of their

results. Our goal is to perform experiments aimed at establishing a link between concentrated solutions of polymeric micelles and colloidal crystals. We illustrate the transition from polycrystallinity to sliding layers in FCC arrays in analogy with the behavior observed in colloidal crystals. The lower density BCC crystals undergo a more continuous deformation of the local lattice that has not been well-documented in colloidal suspensions. In both cases we aim to show that a unified theory should explain the structural transitions in both colloidal and micellar crystals; however, as yet no such model is available.

We use polystyrene/polyisoprene (PS/PI) diblocks suspended in decane, a solvent preferential for polyisoprene, to form micelles comprising a dense core of polystyrene and a diffuse corona of polyisoprene. Previous work in our group centered on understanding intermicellar interactions; self-consistent mean-field calculations suggest that the interaction potential is repulsive.[14] This repulsion arises from the osmotic pressure created upon either interdigitation or compression of coronal chains at center-to-center separations less than the overall diameter of the micelle. Manipulating the diblock degree of polymerization and block asymmetry, we create spherical micelles with varying internal architectures. These differences are responsible for changes in the overall length scale of the repulsion. These micelles undergo disorder–order transitions from liquid-like suspensions to crystalline arrays by increasing the polymer concentration. Experimental diffraction confirms the selection of either body-centered cubic (BCC) or face-centered cubic (FCC) crystals depending on the length scale of the osmotic pressure-driven repulsion.[15]

One interesting feature of these polymeric, micellar crystals is that the hydrodynamic radius is essentially the same as the nearest-neighbor lattice spacing even for BCC crystals. Because these crystals interact strongly thermodynamically and hydrodynamically at the same length scale, one cannot *a priori* anticipate their microstructural evolution when subjected to a steady shear. Secondly, the phase behavior is dictated by polymeric interactions, giving an interaction poten-

---

[†] Stanford University.
[‡] Exxon.
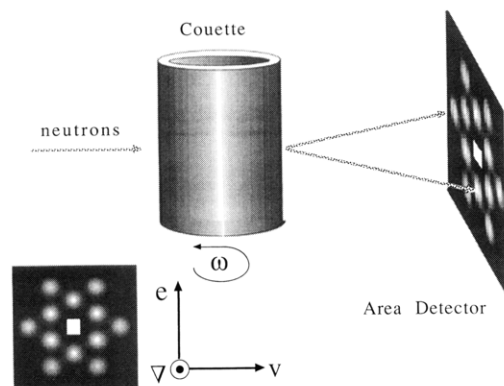
Figure 1. Scattering geometry for experiments. Note that the beam is coincident with the direction of the shear gradient (∇). The beam passes through the couette twice, sampling the velocity vector (**v**) pointing horizontally in both directions. The vertical direction (**e**) is parallel with the vorticity vector.

tial whose form is different than that of charged colloids, but sharing the common feature that their interactions are repulsive. The striking similarity between the microstructural evolution of polymeric micellar crystals under steady shear presented here and the mechanisms first described by Ackerson suggest that the nature of these microstructural evolutions may in fact have some universal features.

2. Experimental Section

The polymers used in this investigation were 33 000/22 000 and 40 000/40 000 molecular weight deuterated polystyrene/polyisoprene (d-PS/PI) diblocks suspended in a mixture of deuterated and hydrogenated decane. The diblocks were synthesized by a well-established anionic polymerization technique.[16] Concentrated suspensions were placed in an oven at no more than 50 °C under vacuum for approximately 1 day to facilitate dissolution. The samples were allowed 4 days or more to equilibrate at room temperature. All experiments reported here were performed at room temperature. Suspending d-PS/PI diblocks in decane comprising 10.7 mol % deuterated decane matches the scattering density of the solvent to that of polyisoprene so that the scattering intensities measured depend only on the spherical, dense (deuterated) polystyrene cores and their spatial correlations. Previous work by our group identified the disorder–order transitions in these micellar suspensions.[15] We use the 33K/22K PS/PI diblocks because the micelles form face-centered cubic crystals at a total polymer concentration of 15% by weight. At 10 weight % the micelles formed from 40K/40K PS/PI diblocks are organized in a body-centered cubic crystal. These are concentrations slightly above the disorder–order transition where previous experiments demonstrate clean diffraction results.

The small angle diffraction experiments were performed at the National Institute of Standards and Technology reactor division. Data were collected on an area sensitive detector at the NG7 (NIST/Exxon/U. Minn/Texaco) SANS Beamline, with sample to detector distances of 7.5 and 11 m. The nominal wavelength of the neutrons was 7.00 Å with a dispersity $\Delta\lambda/\lambda$ of 0.10 and an average incident intensity of approximately 35 000 neutrons/s. The accessible range in q, the magnitude of the scattering vector defined by $(4\pi/\lambda) \sin (\theta/2)$, included 0.0060–0.0504 and 0.005–0.040 Å^{-1}, respectively. A small aperture of approximately 1 cm in diameter was placed before the sample to limit the width of the diffraction spots. The micellar crystal samples were placed inside a couette designed for SANS experiments.[17] This quartz couette consists of a fixed diameter rotor with several choices for the internal stator. We chose a stator offering a 0.3 mm gap width in order to minimize multiple scattering. The gap width to nominal radius was 0.006, providing uniform, linear shear. The resulting scattering configuration for the steady shear experiments is outlined in Figure 1. The incident flux coincides with the

direction of the shear gradient (∇). When viewing a two-dimensional diffraction image from this configuration, the velocity vector (**v**) is in the horizontal direction while the vertical direction is parallel to the vorticity vector (**e**). The diffraction images represent the steady shear microstructure at the prescribed shear rate averaged over a 10–15 min integration time. Experiments allowed a 15 min time interval between shear rates for transient response to changing shear rates. All indications of transient response disappear within the first 5 min after a jump in shear rate.

The steady shear stress versus shear rate data were collected from a constant shear rate rheometer. A constant shear rate RDA II Rheometrics rheometer was equipped with a couette. The couette gap width was 1 mm, and the ratio of gap width to nominal radius was less than 0.04, again within the linear shear regime. The sample was presheared at 50 s^{-1} and allowed to equilibrate for 30 min. The steady stress represents the average value from a 3 min interval with 3 min intervals between changing shear rates and data averaging to allow for transient effects. A preliminary shear rate jump monitoring the transient shear stress showed that it reached 98% of its steady state value within 3 min. The experiment with increasing shear rates was performed independently of the experiment with decreasing shear rates. A 30 min equilibration period was allowed between shear sweeps to minimize memory effects. The shear rates accessed in this experiment ranged from 0.001 to 100 s^{-1}.

3. Results and Discussion

3.1. Scattering Theory. In this section we will present the most general expressions for the intensity arising from coherent small angle scattering experiments. This section aims at separating the contributions from the intraparticle and interparticle scattering to the total scattered intensity. The separation of these contributions to the total scattered intensity facilitates our discussion of the long range order in polymeric micellar crystals.

The most basic expression for the differential cross section per unit volume,[18] referred to here as the scattered intensity, is

$$I(\mathbf{q}) = \frac{1}{V}\langle\sum_{i=1}^{N}\sum_{j=1}^{N}F_i^*(\mathbf{q})F_j(\mathbf{q}) \exp[i\mathbf{q}\cdot(\mathbf{r}_i - \mathbf{r}_j)]\rangle \quad (1)$$

where the scattering amplitude, $F(\mathbf{q})$, accounts for the intraparticle interference and i and j represent sums over different particles. Here, the * superscript stands for the complex conjugate. A simple integral expression fully describes the scattering amplitude

$$F_i(\mathbf{q}) = \int_0^\infty [\varrho_{sol} - \varrho_i(\mathbf{r})] \exp(i\mathbf{q}\cdot\mathbf{r}) \, d\mathbf{r} \quad (2)$$

where $\varrho_i(\mathbf{r})$ represents the spatially varying scattering length density and ϱ_{sol} represents the scattering length density of the solvent. For monodisperse systems where species i and j are identical, the expression for the scattered intensity simplifies to

$$I(\mathbf{q}) = \left(\frac{N}{V}\right)F(\mathbf{q}) \, F^*(\mathbf{q}) \left(\frac{1}{N}\langle\sum_{i=1}^{N}\sum_{j=1}^{N} \exp[i\mathbf{q}\cdot(\mathbf{r}_i - \mathbf{r}_j)]\rangle\right) \quad (3)$$

Typically, the product of the scattering amplitude with its complex conjugate is grouped together, defining the particle form factor. When the particle exhibits spherical symmetry, the scattering amplitude is real and the form factor equals the square of the scattering amplitude

$$P(q) = F^2(q) = \left[4\pi\int_0^\infty(\varrho(r) - \varrho_{sol})r^2\frac{\sin(qr)}{qr} \, dr\right]^2 \quad (4)$$

The remaining portion of eq 3 is traditionally defined

as the structure factor incorporating all interparticle correlations

$$S(\mathbf{q}) = \frac{1}{N}\Big\langle\sum_{i=1}^{N}\sum_{j=1}^{N}\exp[i\mathbf{q}\cdot(\mathbf{r}_i - \mathbf{r}_j)]\Big\rangle \qquad (5)$$

One benefit of this definition of the structure factor is that for perfectly uncorrelated particles it is exactly unity. The scattered intensity is now reduced to two separate functions with different contributions

$$I(\mathbf{q}) = nP(q)\,S(\mathbf{q}) \qquad (6)$$

where n represents the number density of the particles.

In this paper, we are primarily concerned with the development of the structure factor in the presence of a shear field. The structure factor for these experiments becomes a time-averaged structure factor for the flowing crystals. Since the measured intensity includes contributions from both intra- and interparticle interference, we will first quantify the particle from factor before proceeding with a detailed discussion of the structure factor resulting from micellar crystals under shear.

As stated earlier in the Experimental Section, the micelles are composed of deuterated polystyrene/polyisoprene diblocks suspended in a mixture of hydrogenated and deuterated decane designed to match the scattering density of hydrogenated polyisoprene. The resulting form factor is completely dominated by scattering from the polystyrene cores. The dense cores of polystyrene are well-modeled as a uniform solid sphere, whose scattering amplitude is the first-order spherical Bessel function. The analytical form factor for a constant (scattering length) density sphere has nodes at locations depending on the radius of the sphere. Experimentally, these nodes are smeared by particle and wavelength polydispersity. To account for this, the particle form factor is determined by integrating over a probability distribution function describing either the wavelength or particle dispersity. In our case the micelles are extremely monodisperse[15] and the correction to the form factor depends mainly on incorporating the wavelength polydispersity from the neutrons

$$P_{\text{exp}}(q\bar{\lambda}) = \int_0^{\infty} P(q\lambda)\,G(\lambda)\,\mathrm{d}\lambda \qquad (7)$$

where $\bar{\lambda}$ denotes the mean wavelength. Often, $G(\lambda)$ is described with a Schulz distribution function

$$G(\lambda) = \frac{\lambda^Z}{\Gamma(Z+1)}\left(\frac{Z+1}{\bar{\lambda}}\right)^{Z+1}\exp\left(-\frac{\lambda}{\bar{\lambda}}(Z+1)\right) \qquad (8)$$

Alternatively, one can replace λ with R_c and $\bar{\lambda}$ with $\bar{R}_c$ and attribute the polydispersity index, Z, to polydispersity in the radius R_c.[19,20]

As stated earlier, the structure factor is unity for uncorrelated particles, giving a scattered intensity that depends only on the form factor. Since this is the case for our micelles at dilute concentrations of approximately 0.5 weight % polymer, we can accurately determine the micellar form factor using constant density, solid sphere models subject to the polydispersity distribution function described by eq 8. Figure 2 demonstrates our best fits to these experimental form factors. For micelles formed from 33K/22K diblocks in PI match decane, the best fit form factor has a core radius of 150 Å. The polydispersity index, Z, obtained from this fit is 98. The polydispersity index is related to the standard deviation by
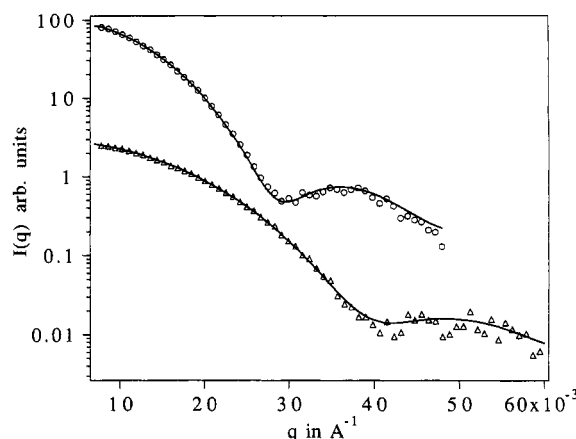
Figure 2. SANS form factors measured at 0.5 weight % polymer for both (O) 33K/22K and (△) 40K/40K micelles in core contrast decane (0.107 mole fraction deuterated n-decane). P-(q) fits (—) to solid spheres subject to a Schulz distribution yield a core radius of 150 Å and a polydispersity index of 98 for the 33K/22K micelles. For the 40K/40K micelles, the core radius is 106 Å with a polydispersity index of 63.

$$\sigma = \frac{1}{(1+Z)^{1/2}} \qquad (9)$$

resulting in a standard deviation of approximately 0.10, a value very close to the standard deviation in wavelength, $\Delta\lambda/\bar{\lambda}$. Our previous experiments show that these micelles have a mean aggregation number of 335 diblocks.[15] Comparing the radius obtained from our form factor fit with the radius obtained from a solid sphere of polystyrene chains yields excellent agreement. This agreement suggests that the cores are less than 10% (by volume) decane. So the cores are in fact quite compact. Additionally, the reasonable agreement between the theoretical form factor and experimental data suggest that the interface between the core and the corona is small relative to the core dimension. Micelles comprising 40K/40K chains have a core radius of 106 Å with a mean aggregation number of 90 diblocks. The polydispersity index obtained from the best fit was 63, corresponding to a standard deviation of $\sigma = 0.125$.

With the intramicellar contribution to the scattered intensity fully specified, we can use SANS diffraction experiments to probe the long range order in micellar crystals under shear flow. We will begin with a general description of the crystalline structure factor before proceeding with quantitative expressions. Bragg diffraction occurs when the sample has crystalline order such that the particles are restricted to positions with fixed periodicity. As a result of this order, eq 5 will have specific values of $\mathbf{q}$ where $\exp(i\mathbf{q}\cdot(\mathbf{r}_i - \mathbf{r}_j))$ is an integer. This constructive interference adds over many particles, giving rise to a Bragg peak. Simple diffraction theory also predicts the shape of this Bragg peak based on a Fresnel construction of the scattering from a finite crystal with M layers. The general expression is[21,22]

$$I_{\text{Bragg}} \propto \frac{\sin^2(\tfrac{1}{2}M(\mathbf{a}_i\cdot\mathbf{q}))}{\sin^2(\tfrac{1}{2}(\mathbf{a}_i\cdot\mathbf{q}))} \qquad (10)$$

Bragg reflections have a half-width proportional to $1/M$ and for large M the reflections are extremely narrow. This equation serves as a generalized equation for the Dirac δ function because as M approaches infinity the half-width approaches zero. In our experiments, where the crystalline unit cell dimension is on the order of 1000 Å and the sample cell is 0.3 mm, the number of layers
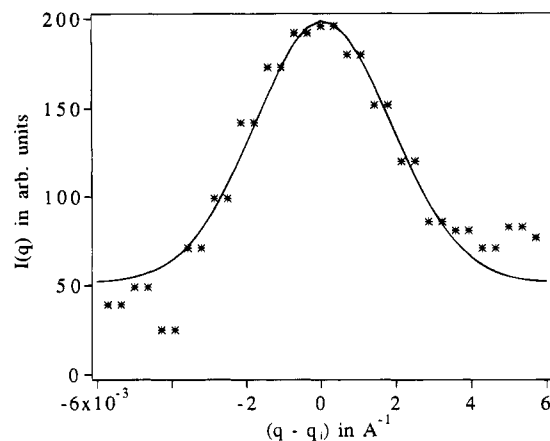
Figure 3. A resolution limited spot (*) from the diffraction of a face-centered crystal composed of 33K/22K micelles at rest after preshearing such that the $\langle 111 \rangle$ planes are stacked along the shear gradient. The diffraction spot is fit (—) to a Gaussian, $I_{Bragg} \propto \exp(-(q - q_i)^2/2\sigma^2)$ with σ equal to 0.0018 Å^{-1}.

can be on the order of several thousand, giving a diffraction peak well approximated by the Dirac δ function. Treating the diffraction peaks as weighted Dirac δ functions provides a valuable simplification in the analysis because SANS diffraction suffers from diffraction-limited spots; that is, the width of the diffraction spots is largely determined by the wavelength distribution and aperture size. The resulting diffraction image becomes a convolution of the theoretical diffraction image with the resolution-limited function

$$I_{exp}(\mathbf{q}) = nP(q)\, S(\mathbf{q}) \bigstar H(q) \tag{11}$$

where $H(q)$ represents this resolution-limited smearing function. Since the diffraction spots are treated as δ functions, they simply sift the smearing function at the Bragg location. By fitting a resolution-limited diffraction spot, we can characterize the smearing function $H(q)$ and apply this to our theoretical models. For simplicity we fit the diffraction spot to a Gaussian, as depicted in Figure 3, to determine the parameters for our smearing function $H(q)$.

3.2. Crystalline Structure Factors. In general, the flowing crystals at moderate shear rates consist of the densest packed planes slipping past each other such that they stack in the direction of the shear gradient. To accommodate the diffraction pattern arising from these flowing crystals, Ackerson and Loose[23] adapted a general diffraction theory for the structure factor resulting from the scattering of layered structures.[24,25] This theory has successfully described FCC colloidal crystals under steady shear. We use this general theoretical framework to fully describe the SANS diffraction images observed for both FCC and BCC micellar crystals under steady shear.

According to Ackerson and Loose,[23] the structure factor arising from crystalline layers has the following form

$$S(\mathbf{q}) = \frac{1}{M}L(\mathbf{q})\Big\langle \sum_{n=1}^{M}\sum_{m=1}^{M} \exp(i\mathbf{q}\cdot(\mathbf{R}_m - \mathbf{R}_n))\Big\rangle \tag{12}$$

where M specifies the number of layers in the crystal and $\mathbf{R}_m$ and $\mathbf{R}_n$ denote the translation vectors that point from the origin within the first layer to the origin in the mth and nth layers, respectively. The layer form factor, $L(\mathbf{q})$, represents the scattering occurring from a

single layer of the crystal. For an infinite, defect-free layer, the layer form factor becomes a sum of δ functions located at the 2-D reciprocal lattice vectors. The ensemble average in the brackets accounts for interlayer interference and depends explicitly on the phase difference between successive layers as defined by the translation vectors. The location of the Bragg peak is determined by the layer form factor, but the magnitude, including the possibility of suppression, is determined by the stacking sequence. We will use this basic formulation to describe the structure factors arising from the scattering of layered micellar crystals.

3.2.1. FCC Micellar Crystals. For face-centered crystals, the $\langle 111 \rangle$ plane is the densest plane. This plane has a 2-dimensional hexagonally close-packed (HCP) structure with a spacing corresponding to the nearest-neighbor distance in an FCC crystal. The real space two-dimensional basis vectors are given by

$$\mathbf{a}_1 = d\mathbf{v} \qquad \mathbf{a}_2 = \frac{d}{2}(\mathbf{v} + \sqrt{3}\mathbf{e}) \tag{13}$$

where d defines the nearest-neighbor distance, $\mathbf{v}$ is the unit vector in the flow direction, and $\mathbf{e}$ represents a unit vector parallel to the vorticity direction. The corresponding reciprocal basis vectors for this 2-D set are

$$\mathbf{q}_1 = \frac{2\pi}{d}\Big(\mathbf{q}_v - \sqrt{\frac{1}{3}}\mathbf{q}_e\Big) \qquad \mathbf{q}_2 = \frac{2\pi}{d}\sqrt{\frac{4}{3}}\mathbf{q}_e \tag{14}$$

The distinction between an FCC crystal and a 3-dimensional HCP structure depends only on the correlation between layers. Two possibilities exist for stacking the subsequent 2-D HCP layers such that the next layer lies in a 3-fold hollow site of the preceding layer. In a perfect FCC crystal the series proceeds as ...ABCAB-CABC... or ...ACBACBACB... for the stacking sequence. These sequences correspond to the two possibilities for the translation vectors

$$\mathbf{r}_1 = d\Big(\frac{1}{2}\mathbf{v} + \sqrt{\frac{2}{3}}\nabla + \frac{1}{2\sqrt{3}}\mathbf{e}\Big)$$

$$\mathbf{r}_2 = d\Big(\frac{1}{2}\mathbf{v} + \sqrt{\frac{2}{3}}\nabla - \frac{1}{2\sqrt{3}}\mathbf{e}\Big) \tag{15}$$

An FCC twin arises when a mirror plane exists such that the sequence ...ABCABCBACBA... might occur, representing one twin plane in an otherwise perfect FCC crystal. A 3-D HCP structure has greater interlayer order than FCC with a sequence alternating between layers with only one registry site. A series of either ...ABABABAB... or ...ACACACAC... represents a perfect 3-D HCP. The presence of the mirror plane in the FCC twin mimics the 3-D HCP structure for three layers. When an FCC crystal is highly twinned, containing many mirror planes, the crystal is actually somewhere between an FCC and 3-D HCP structure. Ackerson and Loose developed an expression for the structure factor of a faulted crystal composed of 2-D HCP layers to account for the degree of twinning using a stochastic transfer matrix approach. In this expression,

$$S(\mathbf{q}) = L(\mathbf{q})\{a(1-a)[1 - \cos\mathbf{q}\cdot(\mathbf{r}_1 - \mathbf{r}_2)]\}/$$
$$\{1 - 2a + 3a^2 - 2a^2(\cos\mathbf{q}\cdot\mathbf{r}_1 + \cos\mathbf{q}\cdot\mathbf{r}_2) +$$
$$a^2\cos\mathbf{q}\cdot(\mathbf{r}_1 - \mathbf{r}_2) + (2a - 1)\cos\mathbf{q}\cdot(\mathbf{r}_1 + \mathbf{r}_2)\} \tag{16}$$

when $a = 1$, one has a perfect FCC crystal and, when $a = 0$, one obtains a perfect 3-D HCP crystal. Special consideration must be taken when evaluating this
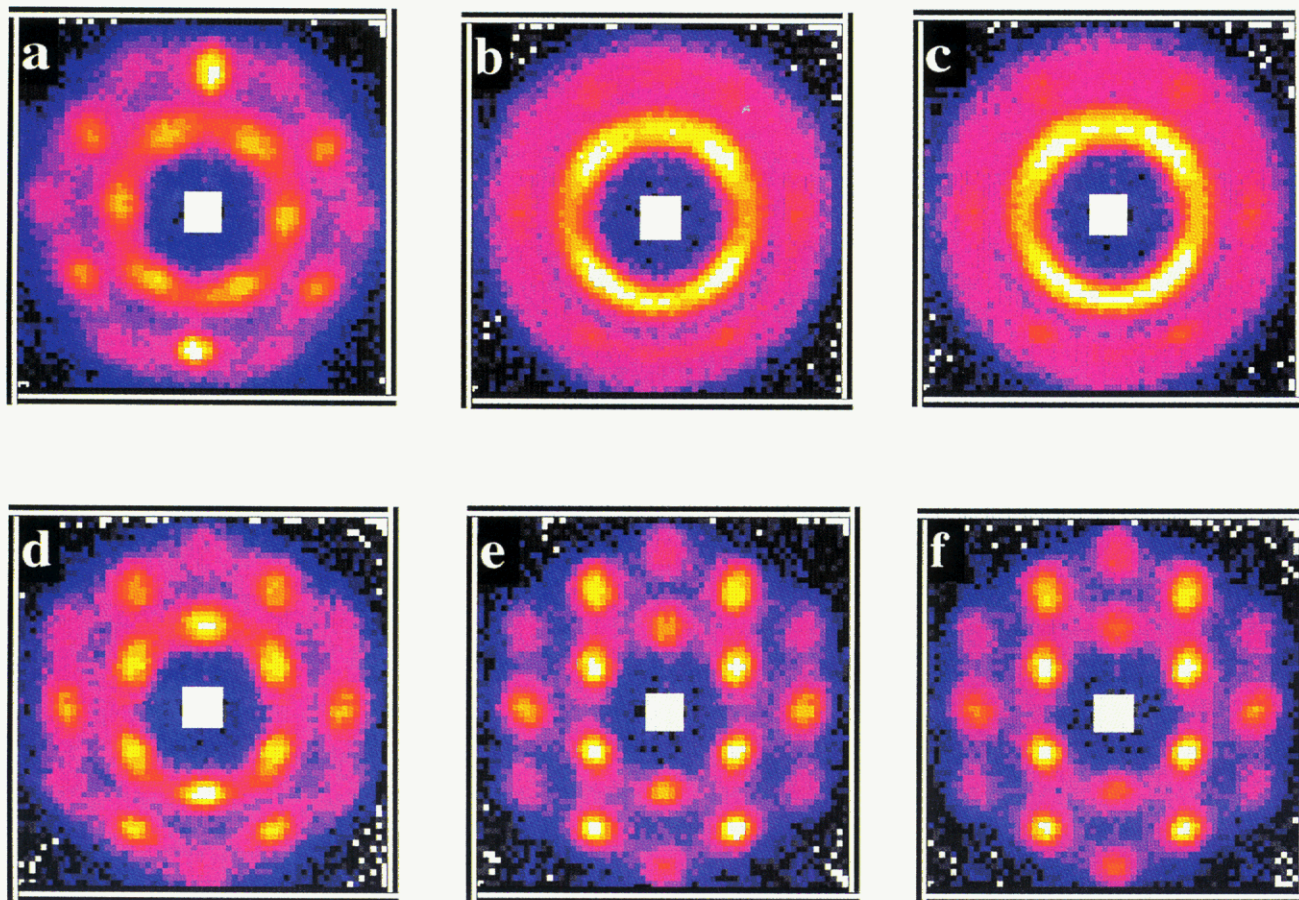
Figure 4. Experimentally measured diffraction images taken at various steady shear rates, $\dot{\gamma}$, for FCC micelles formed from 33K/22K diblocks at 15 weight % suspended in core contrast decane: (a) $\dot{\gamma} = 0.00$ s^{-1}, aligned by inserting stator; (b) $\dot{\gamma} = 0.06$ s^{-1}; (c) $\dot{\gamma} = 0.66$ s^{-1}; (d) $\dot{\gamma} = 6.60$ s^{-1}; (e) $\dot{\gamma} = 66.0$ s^{-1}; (f) $\dot{\gamma} = 200.0$ s^{-1}. For these experimental diffraction images $\mathbf{q}_v$ and $\mathbf{q}_e$ range from +0.0280 to −0.0280 Å^{-1}.

expression when the ratio is indeterminate. These details are clearly identified by Loose and Ackerson.[23] The effect of modulating the Bragg peaks in close-packed crystals with different stacking sequences can be quite dramatic. In fact, for certain stacking sequences the interlayer interference can cause complete suppression of specific Bragg reflections.

Previous experiments with micelles formed from 33K/22K diblocks in decane at this concentration show the equilibrium structure is a face-centered cubic crystal with a lattice constant of 984 Å. After the sample was placed in the rotor and the stator was inserted, creating a transient vertical shear, the sample was allowed to rest for 15 min and the diffraction image in Figure 4a was acquired. Equation 16 can be used to describe the crystal structure factor resulting from the shear-induced orientation. The model of the scattering pattern is best approximated by a highly twinned FCC crystal with ⟨111⟩ planes aligned perpendicular to the beam and a = 0.5, as shown in Figure 5a. The decay in the form factor at higher q prevents resolution of the higher order diffraction spots. The polystyrene core radius is 150 Å, giving a first node in the form factor at 0.03 Å^{-1}. When $a = 1$, a perfect FCC crystal, one translation vector describes the formation of the two registry sites and this specific stacking sequence causes the interference from the innermost ring to vanish completely. An evaluation of eq 16 bears this result when treated in the limit as a approaches 1. Thus it is trivial to deduce that the structure is twinned to some extent. In fact, a highly twinned structure is expected if one considers the crystal microstructure under flow. As the planes are forced to

slip past each other, there cannot be a high degree of communication between layers. When the flow ceases, the layers relax into the nearest registry sites, giving a highly twinned structure.

A series of steady-state shear diffraction patterns are displayed in Figure 4. Again, each diffraction image signifies a 15 min average with 15 min before data acquisition to allow for transient effects. In the first panel, the crystal is aligned due to the initial vertical shear associated with plunging the stator down into the rotor cup. At shear rates below 3 s^{-1} (see Figure 4b,c), the sample exhibits defect-mediated flow. For these shear rates the shearing motion creates a dynamic network of dislocations that allow crystallites to roll against each other. As the crystallites tumble, they sample orientations different from the ⟨111⟩ planes aligned parallel to the wall. These tumbling crystallites can be thought as having random orientation at any instant in time. As a result, this contribution to the scattered intensity is exactly like that expected from powder-pattern diffraction. The structure factor is an average over the scattering vector q of the three-dimensional reciprocal lattice vectors. Traditionally, the line shape of the Bragg reflection, referred to here as the smearing function, is incorporated such that

$$S(q) \star H(q) = \sum_{q_i} \frac{m_{hkl}}{\sqrt{2\pi}\sigma q q_i} \exp\left(-\frac{(q - q_i)^2}{2\sigma^2}\right) \quad (17)$$

For a three-dimensional FCC crystal the magnitude of the scattering vector q_i is determined from the reciprocal
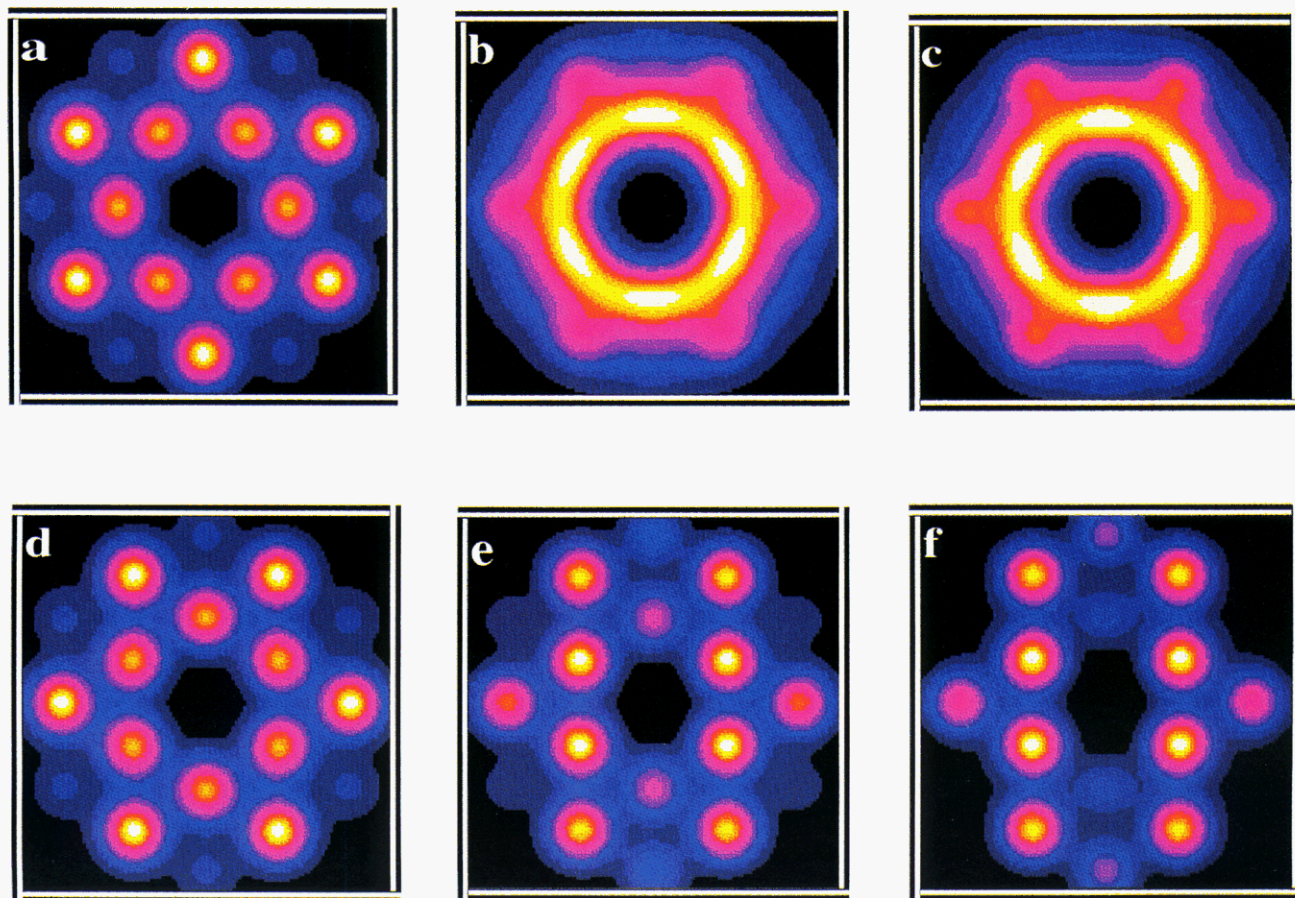
Figure 5. Models of the FCC micellar crystals comprising 33K/22K PS/PI diblocks in core contrast decane with a lattice constant of 984 Å: (a) faulted FCC crystal with $a = 0.5$; (b) coexistence between $\langle 111 \rangle$ planes (20%) and polycrystalline phase (80%); (c) coexistence between $\langle 111 \rangle$ planes (25%) and polycrystalline phase (75%); (d) slipping $\langle 111 \rangle$ planes hopping from registry sites with $C = 0.5$; (e) slipping planes with $C = 0.45$; (f) slipping planes with $C = 0.4$. Again, for these model diffraction images $\mathbf{q}_v$ and $\mathbf{q}_e$ range from 0.028 to -0.028 Å^{-1}.

basis vectors[26]

$$q_i = \frac{2\pi}{A}\sqrt{(h - k + l)^2 + (h + k - l)^2 + (-h + k + l)^2} \tag{18}$$

where h, k, and l are whole integers, m_{hkl} defines the degeneracy of the magnitude for each Bragg peak, and A denotes the lattice constant. Since the set of reciprocal lattice vectors create a lattice in reciprocal space, one way to envision the degeneracy m_{hkl} is to picture the number of reciprocal lattice points at a radius of q in reciprocal space. The value for the degeneracy can easily be computed by determining the number of hkl combinations that give rise to the same magnitude in the scattering vector. It should be noted that, in general, a powder diffraction pattern is isotropic, or one-dimensional, yielding diffraction rings when observed on an area detector.

Describing the resulting diffraction images as a combination of sliding layers and tumbling crystallites allows us to generate models of the observed scattering patterns as shown in Figure 5b,c. The resulting structure factor becomes

$$S(q)\star H(q) =$$
$$(1 - \phi)S_{\text{layer}}(q)\star H(q) + \phi S_{\text{powder}}\star H(q) \tag{19}$$

where $S_{\text{layer}}(\mathbf{q})$ is defined by eq 16 and $S_{\text{powder}}(q)\star H(q)$ is given by eq 17. The quantity ϕ describes the portion of the sample that is polycrystalline, while the remaining portion is assumed to be $\langle 111 \rangle$ layers oriented
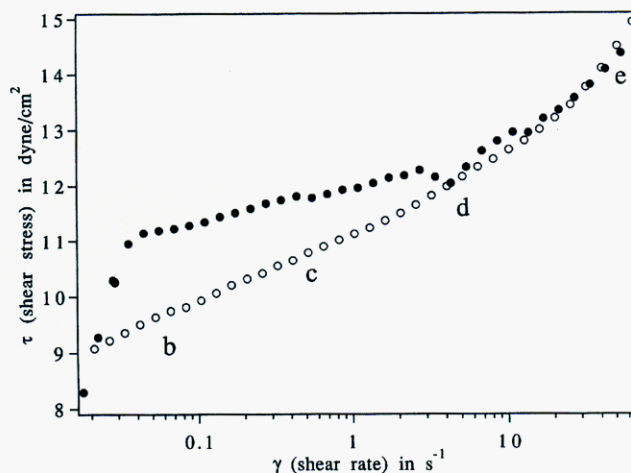
Figure 6. Steady shear stress as a function of constant shear rate for both (●) increasing and (○) decreasing shear rate on an FCC micellar crystal composed of 33K/22K PS/PI diblocks at 15 weight % polymer in *n*-decane.

normal to the shear gradient and slipping past each other in a registry hopping mechanism. Within this approximation, the percentage of sample that becomes slipping layers slowly increases with shear until about 6 s^{-1}. At this shear rate, the entire sample is composed of $\langle 111 \rangle$ layers that slip past each other, as seen in Figure 4d. Experimentally, the structure factor is time-averaged over all configurations for the layers. Since the diffraction image most closely resembles a highly twinned FCC crystal diffraction image observed at zero

shear, we conclude that the layers slip past each other by hopping from one registry site to the next. The particles spend most of their time at one of the registry sites until the layer finally slips, hopping very rapidly to the next registry site. This slip–stop–slip motion would create an image identical to the static, highly twinned FCC if the particles hop to the 3-fold hollow sites. At still higher shear rates, the zigzag motion associated with slipping layers decreases in amplitude, which is to say that the particles do not hop to the 3-fold hollow cites. Ackerson and Loose parameterized the translation vectors to account for decreases in the in-plane oscillations as the particles in neighboring planes slipped past each other. The new translation vectors become

$$\mathbf{r}_1 = d\left(C\mathbf{v} + \sqrt{\frac{2}{3}}\nabla + \frac{1-C}{\sqrt{3}}\mathbf{e}\right)$$

$$\mathbf{r}_2 = d\left(C\mathbf{v} + \sqrt{\frac{2}{3}}\nabla - \frac{1-C}{\sqrt{3}}\mathbf{e}\right) \qquad (20)$$

Of course, when $C = \frac{1}{2}$ this result is equivalent to eq 15. This parameterized set of translation vectors can now be used in eq 16 to determine the modulation to the structure factor. As can be seen in Figures 4e and 5e, at 66 s^{-1}, a value of $C = 0.45$ best models the experimental diffraction image. At 200 s^{-1}, Figures 4f and 5f suggest a value of $C = 0.4$ best models the experimental diffraction. In both cases the diffraction spots along the innermost columns become enhanced.

Modeling the experimental diffraction images leads to a picture of the progression of long range order of FCC crystals under shear. At low shear rates, the flow is defect mediated where the shear field produces crystallites that tumble to allow the sample to flow on a macroscopic level. As the shear increases, the sample undergoes a transition from polycrystallinity to registry hopping $\langle 111 \rangle$ layers. This transition is similar to a first-order phase transition. The ordering field in this transition becomes the shear rate; the paracrystalline phase represents the disordered phase, and the $\langle 111 \rangle$ slipping layers serve as the ordered phase. The system has a miscibility gap causing the order–disorder transition to exhibit coexistence over a finite region. This analogy may not ultimately prove useful because it is limited to a finite range of shear rate. Also, it is not clear that the slipping layers observed at higher shear rates, where the amplitude of the in-plane oscillation is observed to diminish, are equivalent to the registry hopping layers observed at lower shear rates.

More importantly, the effect of this transition can be observed in the stress–shear rate curves obtained from our study of this sample in a Rheometrics couette. The sample shows a great deal of hysteresis over this polycrystalline to slipping layers transition. Figure 6 shows the measured stress acquired from the steady shear rate. The sample was presheared and allowed to rest for approximately 0.5 h. The sample was subsequently subjected to a sweep of increasing steady shear rates where the resulting stress was measured. After the increasing shear sweep, the sample was allowed to rest for another 0.5 h and the sample was subjected to the maximum shear rate and the stress was measured for decreasing values of the steady shear rate. The result of this process produces a portion of the stress–shear rate curve that overlaps and a zone that does not overlap. The steady shear diffraction images

indicate that the overlapping portion of the stress–shear rate curve corresponds to shear rates where the entire sample is composed of $\langle 111 \rangle$ layers slipping past each other. The nonlinearity in stress versus shear rate arises from the fact that as the shear rate increases the amplitude in the zigzag motion diminishes. The hysteresis, on the other hand, results from the polycrystalline to slipping layers transition. We should note that the transition from polycrystallinity to slipping layers was not accompanied by a superanomalous change in rheology. The lack of a discontinuous drop in shear stress may be related to the rate of the shear sweep, which was approximately 6 times faster than sweeps reported by Chen and Zukoski on colloidal crystals.[7,9,10,27] Because the large length scale relaxations associated with the formation and destruction of these polycrystallites are not well understood, it is difficult to speculate whether we should expect superanomalous behavior in this system and we cannot predict how dramatically the rate of the sweep will alter the shape of the hysteresis loop.

The polycrystalline domains can be interpreted as a network of dislocations. This results in the following scaling relationship for the stress in the system[28,29]

$$\tau = K/R^2 \qquad (21)$$

where R is the radius of the crystallite and K is the Frank elastic constant. A sample with many small crystallites has many dislocations, producing a higher stress in the sample. This general scaling relationship indicates that the crystallites nucleated at lower shear rates are smaller than the crystallites formed at higher shear rates upon decreasing shear rate. Apparently, the nucleation of these metastable crystallites depends on the shear rate. Ackerson modified a Smoluchowski theory to explain the forces arising between flowing layers. If we treat the tumbling crystallites as layers interacting only at the interface, then Ackerson's model of flowing layers offers some insights. His modified Smoluchowski theory[3] predicts strong shear thinning, making the energy required to tumble these crystallites shear dependent. The size of the crystallites may depend on a balance between the energy required to create the dislocations and the energy required for crystallites to tumble past each other. The minimum energy defines the metastable crystallite size nucleated at these various shear rates.

3.2.2. BCC Micellar Crystals. In samples containing body-centered cubic (BCC) crystals, we observe a different mechanistic evolution for the microstructural transitions in the presence of steady shear. For the BCC crystal, the $\langle 110 \rangle$ comprises the densest plane. Unlike the FCC crystal, the BCC crystal does not flow by having perfect, uniform layers slip past each other, but involves the formation of a BCC twin structure that produces a kink-mediated flow. While in FCC crystals the layers would hop from one registry site to the next, creating a twinning plane parallel to the $\langle 111 \rangle$ planes, in the BCC crystals the twinning plane is perpendicular to the $\langle 110 \rangle$ plane, producing a series of BCC twin structures that slip along the twinning plane allowing the crystal to advance in portions. These twinning boundaries probably shift in a dynamic manner. In previous experiments,[2,3] Ackerson describes this result for colloidal crystals as a kink-mediated flow. If the sample is presheared at or above this critical shear rate, the initial state of the crystal can be modeled as a twinned BCC crystal. Bates has observed this structure
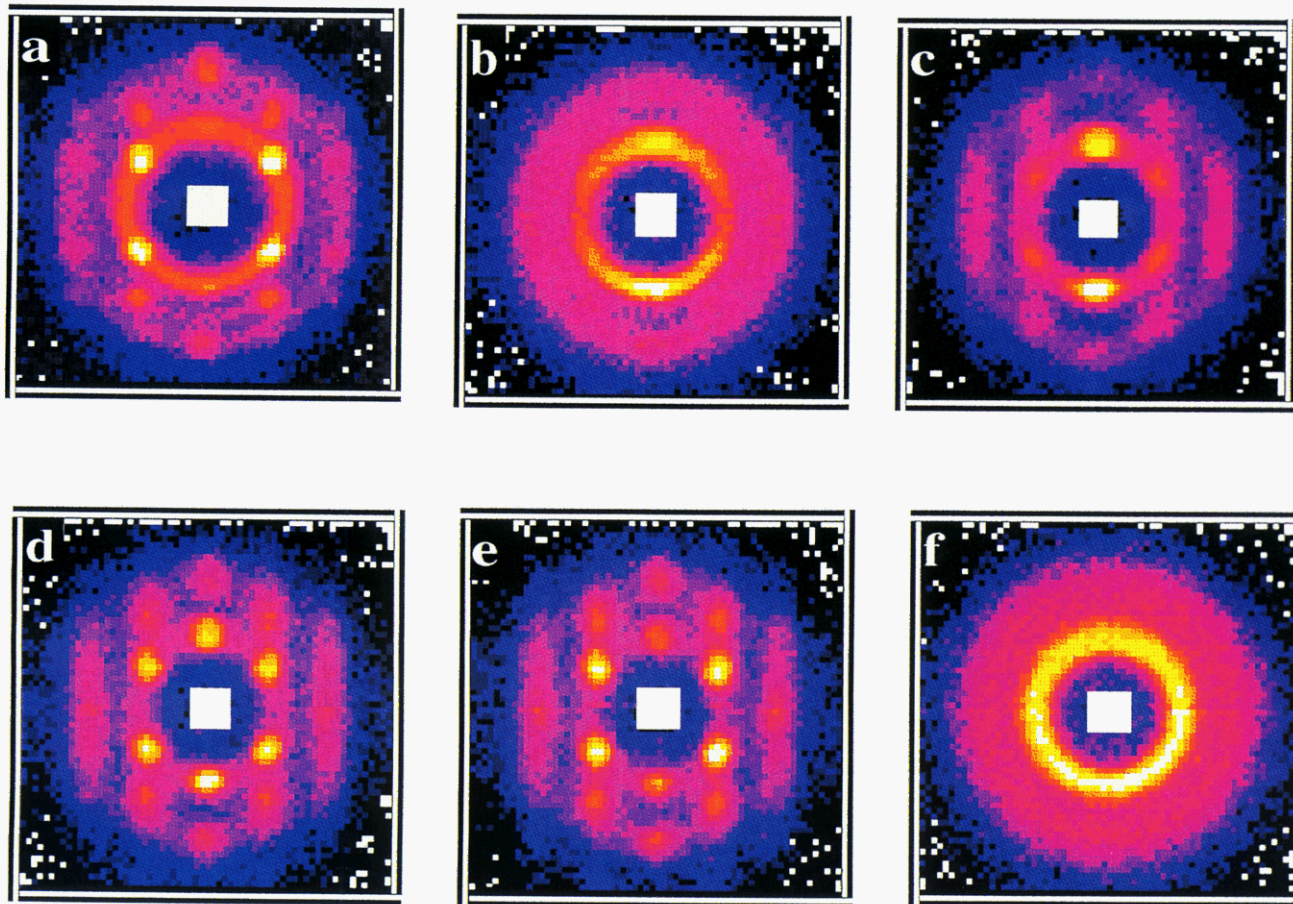
Figure 7. Experimentally measured diffraction images taken at various steady shear rates, $\dot{\gamma}$, for a BCC micellar crystal formed from 40K/40K diblocks at 10 weight % suspended in core contrast decane: (a) $\dot{\gamma} = 0.00$ s^{-1} after subjecting to a preshear above 50 s^{-1}; (b) $\dot{\gamma} = 0.30$ s^{-1}; (c) $\dot{\gamma} = 4.0$ s^{-1}; (d) $\dot{\gamma} = 20.0$ s^{-1}; (e) $\dot{\gamma} = 80.0$ s^{-1}; (f) $\dot{\gamma} = 322.0$ s^{-1}. For these experimental diffraction images $\mathbf{q}_v$ and $\mathbf{q}_e$ range from $+0.036$ to -0.036 Å^{-1}.

in BCC diblock melts subjected to oscillatory shear.[30] We can reconstruct the diffraction image expected for a perfectly twinned BCC crystal with the ⟨110⟩ planes stacked in the direction of the shear gradient by superimposing the diffraction image of each of the two BCC twins. The diffraction pattern expected for a perfect BCC crystal with the ⟨110⟩ normal to the incident beam is given by the following reciprocal lattice vectors

$$\mathbf{q}_1 = \frac{2\pi\sqrt{2}}{A}\mathbf{q}_v \qquad \mathbf{q}_2 = -\frac{\sqrt{2}\pi}{A}\mathbf{q}_v + \frac{2\pi}{A}\mathbf{q}_e \quad (22)$$

such that

$$\mathbf{q}_i = m\mathbf{q}_1 + n\mathbf{q}_2 \qquad (23)$$

For this macroscopic orientation, the BCC crystal is formed by stacking the ⟨110⟩ layers with a single translation vector

$$\mathbf{r}_1 = \frac{A}{2}\mathbf{e} + \frac{A}{\sqrt{2}}\nabla \qquad (24)$$

where again **e** points in the vorticity direction and ∇ points in the direction of the shear gradient. This set of reciprocal lattice vectors and the single translation vector represent the minimum information necessary to construct the two-dimensional structure factor. According to eq 12, we can determine the structure factor for the BCC crystal with this orientation. If we treat the crystal as being infinite, we find that the interference between layers causes all diffraction spots for which m is odd to disappear and all diffraction spots

for which m is even to be reinforced. To account for the second twin, we must determine its orientation relative to the first. As observed in the BCC diblock melt investigated by Bates,[30] the twinned structure for our BCC micellar crystal occurs with each twin offset 35.3° from the direction of the velocity vector, making the closest packed direction in the ⟨110⟩ plane parallel to the velocity vector. Because the reciprocal lattice vectors are always orthogonal to their real space counterparts, a rotation of the real space vectors yields the same rotation of the reciprocal lattice vectors. So we can apply a simple translation of eq 22 to achieve the orientation of each twin and superimpose their results. The first diffraction image in Figure 7a, shows the experimental diffraction achieved after subjecting the crystal to a shear rate above 50 s^{-1}. When modeled as a BCC twin, we obtain the diffraction image displayed in Figure 8a. The presence of the four innermost diffraction spots and the alignment of the spots in the second ring distinguish this as a diffraction image for BCC twins.

A description of the microstructural transitions associated with this BCC micellar crystal under shear is a bit more complicated. Ackerson has observed that the nature of the kink-mediated flow produces strong in-plane stresses that can locally distort the ⟨110⟩ planes, making them appear as 2-D HCP layers. This effect is dramatically observed in the diffraction image obtained at 4.0 s^{-1}, shown in Figure 7d for our micellar system. Since the crystal has only one translation vector, distorting the ⟨110⟩ layers into 2-D HCP will create a
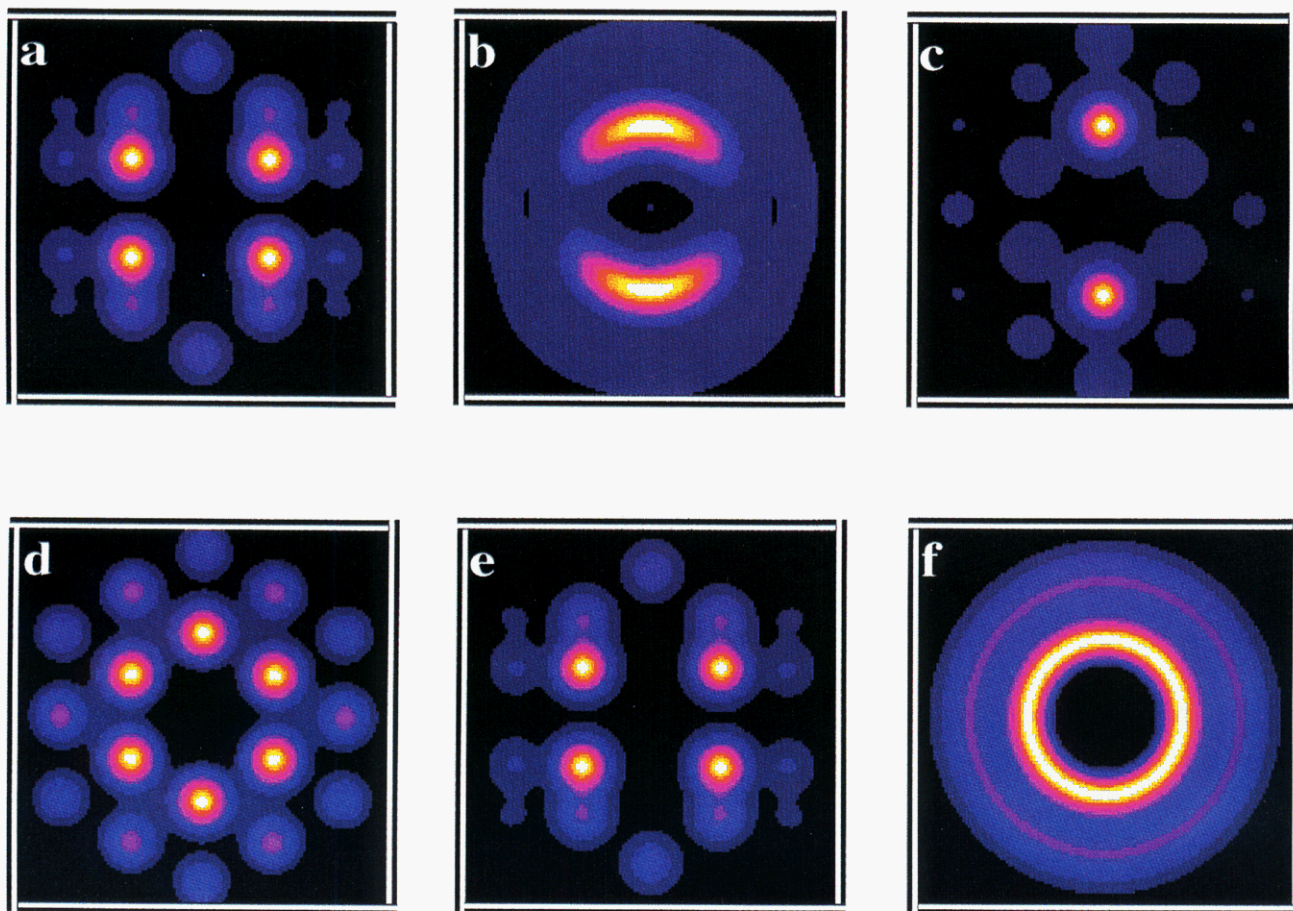
Figure 8. Models of the BCC micellar crystals comprising 40K/40K PS/PI diblocks in core contrast decane with a lattice constant of 598 Å: (a) a twinned BCC crystal with the twinning plane perpendicular to the ⟨110⟩ face; (b) locally distorted ⟨110⟩ plane into a 2-D HCP with paracrystalline distortion and an orientation distribution; (c) locally distorted ⟨110⟩ plane into a 2-D HCP with paracrystalline distortion; (d) locally distorted ⟨110⟩ plane into a 2-D HCP; (e) BCC twin structure as described above; (f) metastable liquid structure at the density of the solid. Again, for these model diffraction images q_v and q_e range from $+0.036$ to -0.036 Å^{-1}.

3-D HCP crystal. We recalculate the in-plane nearest-neighbor distance by assuming the interlayer separation remains unchanged and preserving the number density. For our model, the crystalline structure factor is given by eq 16, now with $a = 0$, as seen in Figure 8d. This gives reasonable agreement with the experimental diffraction pattern. At lower shear rates though (see Figure 7b,c), the image shows two single diffraction spots opposite one another. These spots occur because the crystal maintains constant spacing in the vorticity direction. We may treat this as a paracrystalline distortion of the HCP structure observed at 20 s^{-1}. Paracrystalline distortion to the structure factor can be incorporated into the theory by altering the layer form factor[31,32]

$$L(\mathbf{q}) = Z_1(\mathbf{q})\, Z_2(\mathbf{q}) \qquad (25)$$

where

$$Z_i(\mathbf{q}) = \frac{1 - |R_k(\mathbf{q})|^2}{1 - 2|R_k(\mathbf{q})|\cos(a_k{\cdot}\mathbf{q}) + |R_k(\mathbf{q})|^2}$$

$$|R_k(\mathbf{q})| = \prod_{j=1}^{2} \exp\left[\frac{1}{2}g_{kj}{}^2(\mathbf{q}{\cdot}\mathbf{a}_j)^2\right]$$

where the g_{kj} represents a distortion tensor

$$g_{kj}{}^2 = \frac{\Delta^2 a_{kj}}{a_j{}^2}$$

whose introduction allows for anisotropic distortion of the crystal in the flow direction. The effect of increasing the paracrystalline distortion along the velocity direction is to diminish the intensity of most of the diffraction spots while retaining the intensity of the diffraction spots along the **e** direction. For example, a comparison of Figures 7c and 8c suggests that the paracrystalline distortion that best models the diffraction observed at 4.0 s^{-1} has $g_{12} = g_{22} = 0.1$ and $g_{11} = g_{21} = 0.3$ for the values of the distortion tensor. This means that the distortion along the flow direction is approximately 2 times the distortion along the **e** direction and this distortion is almost half the nearest-neighbor distance.

At the lowest shear rate investigated here, the sample shows diffraction spots observed at 0.3 s^{-1}, but these spots are much more diffuse. Paracrystalline distortion alone cannot account for this diffraction result. Instead, we must include macroscopic orientation to properly describe this behavior. We model this image as having the paracrystalline distortion observed at 4.0 s^{-1} with an orientation distribution for the crystalline lattice vectors. The dominant orientation is the one observed at the higher shear rates, and so this is the zero angle orientation. Translations of the major axis are defined by a single angle θ. We use a distribution function defined to be maximum at zero which goes to zero for

an angle of $\pm 90°$.

$$P(\theta) = \frac{1}{\sigma\sqrt{2\pi}} \exp\left[-\frac{\theta^2}{2\sigma^2 \cos^2(\theta)} \right] \qquad (26)$$

The resulting structure factor is given by

$$S(q) = 2 \int_{-\pi/2}^{\pi/2} S(q,\theta)\, P(\theta)\, \mathrm{d}\theta \qquad (27)$$

Although this distribution function is entirely empirical, our intent is to capture the nature of the preferred orientations of the crystallographic axes. This model of the diffraction image yields reasonable agreement with the experimental diffraction pattern observed at $0.3\ \text{s}^{-1}$.

Overall, we summarize the progression of microstructural transitions as a more continuous distortion of the BCC crystal. At the lowest shear rates observed, the crystal exhibits both paracrystalline distortion along the shear direction as well as a preferred orientation distribution for the crystallographic axes. As the shear rate increases, the crystal adopts a major crystal orientation but still exhibits anisotropic paracrystalline distortion. At moderate shear rates the crystal shows layer-like flow with the crystal distorted locally as a 2-D HCP. Increasing the shear rate further results in the more traditional kink-mediated flow of BCC twins. Although the transition from a local 2-D HCP structure to kink-mediated BCC twins appears to be a reversal from the experimental observation of Ackerson, we note that these are steady shear results and not oscillatory shear experiments. Also, the BCC colloidal crystals form at very low volume fractions, resulting in a significantly smaller elastic modulus when compared to the BCC micellar crystals. Because of this difference, the microstructural transitions in BCC colloidal crystals are collapsed into a much smaller shear regime, making it more difficult to investigate their initial microstructural transitions. Our experiments on BCC crystals demonstrate a distinctly different mechanism of initial defect flow from FCC crystals. We expect this result to hold true for colloidal crystals as well, although the shear rates where these transitions occur may be unreasonably low from an experimental perspective. As the shear rate increases, the system transforms into the traditional kink-mediated flow of BCC twins. We suspect that as the shear rate increases, the bands representing the BCC twins decrease in size and multiply in number. Once the shear rate increases to a point where the bands are unstable, the sample appears to melt.

When we raised the shear to $322\ \text{s}^{-1}$, we lost long range order, as illustrated in Figure 7f. Past experiments with colloidal crystals suggest that the crystals may shear melt for a shear rate where the steady-state stress approaches some critical value.[9,27] Although the origins of this behavior remain poorly understood, we model this diffraction as a metastable liquid at the volume fraction of the solid. Our previous experiments in the absence of shear[14] for micellar suspensions below the order−disorder transition have allowed us to compare experimental liquid structure factors with theoretical predictions based on the Rogers−Young closure to the Ornstein−Zernike equation. The pairwise interaction potential is based on self-consistent field equations for polymer chains tethered to a spherical interface. For the shear-melted crystal observed at $322\ \text{s}^{-1}$, we use the predicted pairwise potential at the solid density to calculate a liquid structure factor. The resulting liquid

intensity is convolved with the smearing function used in the BCC diffraction models to remain consistent. According to Ackerson,[1] the shear field can produce correlations along the velocity direction, giving a distorted, anisotropic liquid structure factor. If the shear field is strong enough, then the resulting image appears elliptical. For our shear-melted crystal at $322\ \text{s}^{-1}$, the position of the first maximum in the structure factor remains equidistant in magnitude of the scattering vector for all directions; making the correction of structure factor for velocity effects unnecessary.

Although we interpret the image observed at $322\ \text{s}^{-1}$ as a metastable liquid whose structure is acquired from integral equations for equilibrium liquids at the solid density, Harrowell suggests that the apparent shear melting arises from an instability arising from a transverse mode that develops at high shear rates in the flowing layers.[33] In this work, the shear-melting transition is based on a Langevin analysis of the mean-square displacement of the particles in a given layer subjected to the Lindemann criterion. While not specifying the mechanism for layer break-up, these predictions imply that the onset of the instability is inversely proportional to the elastic modulus. Interestingly, Chen's experimental observations on colloidal crystals provide a simple scaling of the critical stresses where many of the microstructural transitions occur.[27] Harrowell speculates that the mechanism for the instability arises from a narrowing in the crystal sheets.[34] For BCC crystals, one envisions bands of BCC twins whose width decreases as the shear rate approaches the shear-melting condition. As a result of this band narrowing, Harrowell predicts line broadening in the diffraction spots along $\mathbf{q}_e$ direction. This line broadening is exactly equivalent to the result expected for finite size effects. A careful comparison of the Bragg line shapes along the $\mathbf{q}_e$ and $\mathbf{q}_v$ directions for shear rates just below the shear-melting condition may offer valuable insight into the mechanism for shear melting.

4. Conclusion

Understanding the nonequilibrium microstructures of ordered systems in the presence of hydrodynamic shear fields still remains an open and active area of research with many poorly understood phenomena. While the nonequilibrium properties of atomic solids represent the most widely understood systems, their behavior spans a tremendous field strength owing to their fast equilibration times, as defined by the particles self-diffusion and interparticle spacing. Micellar and colloidal crystals, on the other hand, have much slower self-diffusion, and the stress is transmitted through the solvent acting directly on individual particles. When these crystals are subjected to shear fields, they exhibit similar microstructural transitions over a much more reasonable shear rate. As a result, experimentalists can access shear rates where shear-induced melting is observed. Pioneering work by Ackerson and others shows that the colloidal crystals undergo a series of microstructural transitions as the shear rate is increased. Our own experiments with micellar crystals confirms a similar phenomenology. Chen, Zukoski, and co-workers first demonstrated that face-centered cubic crystals of essentially hard sphere colloids display defect-mediated flow at low shear rates, forming a polycrystalline network.[8] As the shear rate is increased, the polycrystalline structure transforms into sliding layers. We see similar behavior in FCC micellar crystals. Ackerson's

work details the nature of the sliding layers for both body-centered cubic (BCC) and face-centered cubic (FCC) colloidal crystals. At higher shear rates, the crystals shear melt, forming an amorphous or liquid-like structure. The presence of these microstructural transitions strongly influence their rheological properties. The sliding layer microstructure displays strong shear thinning while the shear melting is associated with a discontinuous shear thickening. Yet, controversy over the origins of the shear-melting phenomena cast doubt on our understanding of the mechanisms that lead to these microstructural transitions.

In principle, nonequilibrium molecular dynamics simulations should address many of the problems associated with the evolution of the crystals microstructure at various steady shear rates. Furthermore, nonequilibrium simulations offer a link to the rheology of crystals under shear flow through Green–Kubo relations.[35] In fact, Stevens and Robbins[11] obtained limited success by modeling charged colloidal particles with a Yukawa interaction potential. Unfortunately, several deficiencies persist in these simulation techniques that prevent a full understanding of these structures and their rheological properties. First, these simulations incorporate a few hundred to a few thousand particles and use periodic boundary conditions to approximate bulk properties. The finite-size effects prevent simulations from capturing large wavelength fluctuations found in crystals at low shear rates. So, the defect-mediated flow where polycrystalline domains deform and rotate in the shear field, yet order on length scales of the lattice dimension, remains undisturbed and cannot be modeled with the simulations. Secondly, current simulations ignore hydrodynamic interactions, meaning the effects caused by disturbance fields of other particles must be negligible. For micellar crystals hydrodynamic interactions are important. The extent to which these hydrodynamic interactions either stabilize or destabilize the microstructural transitions are at the root of the shear-melting controversy. Ackerson and others have suggested that shear melting is largely a Brownian effect.[2,11] The time scale for the flow, the inverse shear rate, becomes faster than the time scale for the system to relax through a purely diffusive process, defined as the time it takes a particle to relax a typical interparticle spacing. Boersma and co-workers[36] argue that a fluid instability disrupts the local environment, destroying the sliding layer microstructure, yielding a liquid-like structure. Finally, the simulations are based on a dimensionless shear rate. In order to provide physically significant results, we must be able to define the appropriate time scale for reducing the shear rate. Stevens and Robbins suggest that this time scale is defined by a ratio of the particle radius squared to the self-diffusion coefficient. Yet Chen[27] cannot normalize his rheological data for various colloidal crystals by making the shear rate dimensionless with this time scale. Theoretical work by Brady[37] on colloidal liquids suggests that the time scale is defined by the interparticle separation squared, divided by a short wavelength diffusion coefficient. For liquids, this diffusion coefficient is well-defined because the structure factor approaches unity in this limit. For crystals, this quantity is not well-defined. Until the diffusion coefficient in crystalline solids is properly

defined, no suitable time scale exists for describing and predicting the rheology of these crystalline samples under steady shear.

References and Notes

(1) Clark, N. A.; Ackerson, B. *Phys. Rev. Lett.* **1980**, *44*, 1005.
(2) Ackerson, B. J.; Clark, N. A. *Phys. Rev. Lett.* **1981**, *46*, 123.
(3) Ackerson, B. J.; Clark, N. A. *Physica A* **1983**, *118*, 221.
(4) Ackerson, B.; Clark, N. *Phys. Rev. A* **1984**, *30*, 906.
(5) Ackerson, B. J.; Hayter, J. B.; Clark, N. A.; Cotter, L. *J. Chem. Phys.* **1986**, *84*, 2344.
(6) Liu, J.; Weitz, D.; Ackerson, B. *Phys. Rev. E* **1993**, *48*, 1106.
(7) Chen, L.; Zukoski, C. *Phys. Rev. Lett.* **1990**, *65*, 44.
(8) Chen, L.; Zukoski, C.; Ackerson, B.; Hanley, H.; Straty, G.; Barker, J.; Glinka, C. *Phys. Rev. Lett.* **1992**, *69*, 688.
(9) Chen, L.; Chow, M.; Ackerson, B.; Zukoski, C. *Langmuir* **1994**, *10*, 2817.
(10) Chen, L.-B.; Zukoski, C. F. *J. Chem. Soc., Faraday Trans.* **1990**, *86*, 2629.
(11) Stevens, M. J.; Robbins, M. O. *Phys. Rev. E* **1993**, *48*, 3778.
(12) Mortensen, K.; Brown, W.; Norden, B. *Phys. Rev. Lett.* **1992**, *68*, 2340.
(13) Phoon, C.; Higgins, J.; Allegra, G.; van Leeuwen, P.; Staples, E. *Proc. R. Soc. London A* **1993**, *442*, 221.
(14) McConnell, G. A.; Lin, E. K.; Gast, A. P.; Huang, J. S.; Lin, M. Y.; Smith, S. D. *Faraday Discuss. Chem. Soc.* **1994**, *98*, 349.
(15) McConnell, G. A.; Gast, A. P.; Huang, J. S.; Smith, S. D. *Phys. Rev. Lett.* **1993**, *71*, 2102.
(16) Noda, I., Rubingh, D., Ed.; *Polymer Solutions, Blends, and Interfaces*; Elsevier: Amsterdam, 1992; pp 43–64.
(17) Straty, G.; Hanley, H.; Glinka, C. *J. Stat. Phys.* **1991**, *62*, 1015.
(18) Kotlarchyk, M.; Chen, S.-H. *J. Chem. Phys.* **1983**, *79*, 2461.
(19) Bartlett, P.; Ottewill, R. *J. Chem. Phys.* **1992**, *96*, 3306.
(20) Aragon, S.; Pecora, R. *J. Chem. Phys.* **1976**, *64*, 2395.
(21) Warren, B. *X-Ray Diffraction*; Addison-Wesley: Reading, MA, 1969.
(22) Guinier, A. *X-Ray Diffraction in Crystals, Imperfect Crystals, and Amorphous Bodies*; W. H. Freeman and Co.; San Francisco, 1963.
(23) Loose, W.; Ackerson, B. J. *J. Chem. Phys.* **1994**, *101*, 7211.
(24) Hendricks, S.; Teller, E. *J. Chem. Phys.* **1942**, *10*, 147.
(25) Paterson, M. *J. Appl. Phys.* **1952**, *23*, 805.
(26) Kittel, C. *Introduction to Solid State Physics*; 5th ed.; John Wiley and Sons, Inc.: New York, 1976.
(27) Chen, L. B. *The Dynamic Properties of Concentrated Charge Stabilized Suspensions.* Ph.D. thesis, University of Illinois at Urbana–Champaign, 1991.
(28) Larson, R.; Mead, D. *J. Rheol.* **1989**, *33*, 1251.
(29) Larson, R. G.; Doi, M. *J. Rheol.* **1991**, *35*, 539.
(30) Almdal, K.; Koppi, K. A.; Bates, F. S. *Macromolecules* **1993**, *26*, 4058.
(31) Hosemann, R.; Bagchi, S. *Direct Analysis of Diffraction by Matter*; North-Holland Publishing Co.: Amsterdam, 1962.
(32) Hashimoto, T.; Kawamura, T.; Harada, M.; Tanaka, H. *Macromolecules* **1994**, *27*, 3063.
(33) Harrowell, P.; Fixman, M. *J. Chem. Phys.* **1987**, *87*, 4154.
(34) Harrowell, P. *Phys. Rev. A* **1990**, *42*, 3427.
(35) Evans, D. *Computer Modelling of Fluids, Polymers and Solids*; Plenum: New York, 1990.
(36) Boersma, W.; Baets, P.; Laven, J.; Stein, H. *J. Rheol.* **1991**, *35*, 1093.
(37) Brady, J. F. *J. Chem. Phys.* **1993**, *99*, 567.

MA950491L